GEOLOGY

A modern pulse of ultrafast exhumation and diachronous crustal melting in the Nanga Parbat Massif

Victor E. Guevara[1]*, Andrew J. Smye[2], Mark J. Caddick[3], Michael P. Searle[4,5], Telemak Olsen[6], Lisa Whalen[3], Andrew R. C. Kylander-Clark[7], Michael J. Jercinovic[8], David J. Waters[4,5]

We combine monazite petrochronology with thermal modeling to evaluate the relative roles of crustal melting, surface denudation, and tectonics in facilitating ultrafast exhumation of the Nanga Parbat Massif in the western Himalayan syntaxis. Our results reveal diachronous melting histories between samples and a pulse of ultrafast exhumation (9 to 13 mm/year) that began ~1 Ma and was preceded by several million years of slower, but still rapid, exhumation (2 to 5 mm/year). Recent studies show that an exhumation pulse of similar timing and magnitude occurred in the eastern Himalayan syntaxis. A synchronous exhumation pulse in both Himalayan syntaxes suggests that neither erosion by rivers and/or glaciers nor a pulse of crustal melting was a primary trigger for accelerated exhumation. Rather, our results, combined with those of recent studies in the eastern syntaxis, imply that larger-scale tectonic processes impose the dominant control on the current tempo of rapid exhumation in the Himalayan syntaxes.

INTRODUCTION

The physical and thermal evolution of mountain belts is governed by the interplay between tectonic deformation, the production and transfer of heat, crustal metamorphism, and surface denudation. The extent to which surficial processes (e.g., climate and erosion) can modulate deep crustal metamorphic and tectonic processes is poorly known (*1*–*3*). The places on Earth where surface denudation is most likely to exert control on deeper crustal processes are the syntaxial massifs of the Himalaya—the Namche Barwa massif (NBM) in the east and the Nanga Parbat massif (NPM) in the west (Fig. 1). These fault-bounded, antiformal massifs are characterized by extreme topographic relief (~7000 m) and contain the youngest exposed migmatites and granites on Earth, with metamorphic and melt crystallization ages as young as 0.7 million years (Ma) (*4*–*6*). These ages imply exhumation rates up to 8 to 13 mm/year (*4*, *7*, *8*)—the fastest known intracontinental exhumation rates on the modern Earth.

Competing hypotheses have been proposed to explain ultrafast exhumation in these massifs (Fig. 2). In the "Tectonic Aneurysm" paradigm, extreme surface denudation—driven by fluvial incision of the powerful Indus and Tsangpo Rivers and augmented by glacial erosion—induces rock uplift and exhumation, enhanced by crustal weakening due to decompression melting (*3*, *9*). However, more recent studies suggest a "bottom-up" driver for rapid exhumation, in which tectonic and/or rheologically controlled crustal flow and rock uplift dictate the loci of enhanced surface denudation and crustal exhumation (*4*, *8*, *10*–*13*). Such bottom-up mechanisms include (i) crustal weakening in response to partial melting (*4*) and (ii) changes in far-field tectonic stresses and structural geometry of the orogen that direct crustal flow to the syntaxes, driving localized deformation and uplift (*11*, *12*, *14*). Distinguishing whether initiation of ultrafast exhumation in the Himalayan syntaxes is dominantly driven by changes in surficial, deep crustal, or far-field tectonic processes is central to understanding the extent to which these processes can modulate each other.

Here, we present a petrochronologic study of the NPM in which we assess the temporal relationships between metamorphism, crustal melting, and ultrafast exhumation. Although robust constraints have been placed on the timing of melt crystallization in the NPM, the timing and duration of partial melting of migmatites now exposed at the surface are less well constrained because of ambiguity in the reactions and pressure-temperature (*P*-*T*) conditions from which dated minerals grew. Such petrochronologic constraints are necessary to deduce the exhumation and cooling paths experienced by these rocks, and to evaluate the relative roles of crustal melting, surface denudation, and tectonics in the development of the syntaxial massifs in the Himalaya.

We present data from two rock samples from the core of the NPM, in which radiometric dates from monazite are linked to the petrologic evolution of the studied samples. We use our data in conjunction with previously published *P*-*T* and geochronologic constraints (*4*), as well as new thermobarometric calculations, to reconstruct the pressure-temperature-time (*P*-*T*-*t*) path and melting and crystallization histories of the studied samples. Using a one-dimensional (1D) thermal model, these *P*-*T*-*t* data are used to constrain a permissible range of exhumation histories. We discuss the implications of our results for the relative roles of surface denudation, crustal melting, and structural and tectonic forcing in dictating the tempo of rapid exhumation in the NPM.

RESULTS

Sample descriptions and petrology

We analyzed two rock samples that were collected as float from the Rakhiot glacier, immediately below the summit cliffs of Nanga Parbat and Rakhiot summit (~4500-m elevation; see sample locality

[1]Geology Department, Amherst College, 220 South Pleasant Street, Amherst, MA 01002, USA. [2]Department of Geosciences, Pennsylvania State University, 332 Deike Building, University Park, PA 16802, USA. [3]Department of Geosciences, Virginia Tech, 4044 Derring Hall, 926 W. Campus Drive, Blacksburg, VA 24061, USA. [4]Department of Earth Sciences, University of Oxford, South Parks Road, Oxford OX1 3AN, UK. [5]Oxford University Museum of Natural History, Parks Road, Oxford OX1 3PW, UK. [6]Geology Department, Western Washington University, 516 High Street, Bellingham, WA 98225, USA. [7]Department of Earth Science, University of California, Santa Barbara, 1006 Webb Hall, Santa Barbara, CA 93106, USA. [8]Department of Geosciences, University of Massachusetts, 627 North Pleasant Street, Amherst, MA 01003, USA.
*Corresponding author. Email: vguevara@amherst.edu

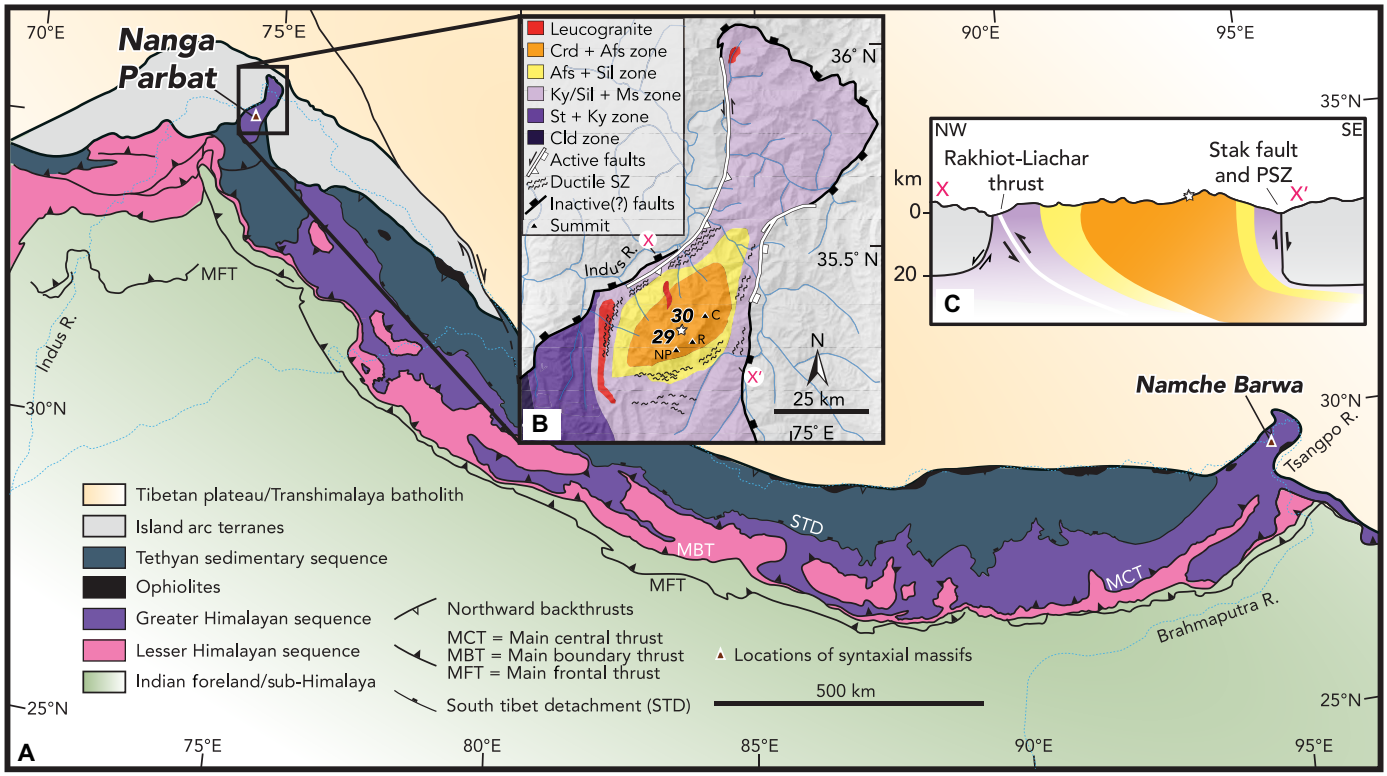

Fig. 1. Geologic setting. (**A**) Simplified geologic map of the Himalaya showing the dominant lithologic units (grouped here according to structural definition) and large-scale structures. Modified after (*78*), with permission from Canadian Science Publishing or its licensors. (**B**) Simplified geologic map of the NPM showing metamorphic isograd zones, leucogranites, major faults and shear zones (SZ), notable mountain summits (NP, Nanga Parbat; RP, Rakhiot Peak; C, Chongra), and sample locations (indicated by white stars; the K-94- prefix to sample numbers referred to in the text has been omitted). Modified after (*63*) with permission from the Geological Society of London, with interpretations from (*4*). Thick white lines indicate known neotectonic faults. List of mineral isograd abbreviations: Afs, K-feldspar; Cld, chloritoid; Crd, cordierite; Ky, kyanite; Ms, muscovite; Sil, sillimanite; St, staurolite. (**C**) Schematic cross section of the NPM modified after (*66*) with permission from Cambridge University Press. Location of the cross section is shown in (B) (lines X and X′). White stars indicate approximate sample locations. PSZ, Phuparash Shear Zone. See (*63*) for details.

map reported in fig. S1), near Nanga Parbat Base Camp. Local topography restricts the bedrock origin of the samples to the summit cliffs of Nanga Parbat that define the core of the NPM, where the highest–metamorphic grade, cordierite-K-feldspar-sillimanite–bearing rocks are exposed (Fig. 1B and fig. S1).

Sample K-94-30 is a restitic pelite characterized by porphyroblastic garnet and K-feldspar. Aligned and elongated biotite, sillimanite, spinel, apatite, corundum, and plagioclase feldspar define a folded foliation (Fig. 3, A and B, and figs. S2 and S3). The presence of corundum and lack of quartz and muscovite suggest that this rock may have undergone complete muscovite breakdown melting with subsequent melt loss, resulting in a silica-undersaturated composition (*15*). Rims of K-feldspar on resorbed biotite, apatite, plagioclase, spinel, and sillimanite (Fig. 3A), and the inclusion of those minerals in porphyroblastic K-feldspar and garnet (Fig. 3B), and in garnet rims enriched in Cr (Fig. 3C), suggest the growth of garnet and K-feldspar during biotite breakdown melting (*16*). Randomly oriented biotite and plagioclase surrounding resorbed garnet and K-feldspar likely grew during cooling and retrograde reaction between garnet, K-feldspar, and melt. Garnet is strongly zoned in major elements: Garnet cores are enriched in Ca and Mn, garnet mantles have lower Ca and higher Mg than the cores, and garnet rims have higher Ca and Fe than the mantles. Zones of high Cr concentrations correlate with high Ca rims and suggest that high-Ca rims may have grown during mica breakdown melting, as discussed above (Fig. 3C). Garnet edges are enriched in Mn and Mg. The strong Mn enrichment in garnet cores suggests that the original growth compositions of garnet have not experienced substantial diffusional modification (*17*, *18*).

Monazite grains in K-94-30 occur as inclusions in high-Ca garnet rims, high-Ca plagioclase rims, K-feldspar, and retrograde biotite. In all textural locations, monazite is located proximal to or in contact with rounded and resorbed apatite and plagioclase (Fig. 3, D to F). The shapes of monazite included in high-Ca plagioclase overgrowths mimic the outlines of the irregular boundaries between low-Ca cores and high-Ca rims (Fig. 3G). Most grains exhibit high-Y, low-Th cores surrounded by low-Y, high-Th overgrowths (Fig. 3G and fig. S3). Some grains exhibit thin (<5-μm-thick) high-Y rims that surround the low-Y mantles.

Sample K-94-29 was originally studied in (*4*). It comprises the leucosome of a migmatitic orthogneiss and contains garnet, quartz, sillimanite, biotite, plagioclase, K-feldspar, and cordierite. Garnet and K-feldspar in this rock were interpreted to have grown during biotite breakdown melting that occurred during exhumation through a very narrow depth window, as the rocks underwent a reaction that produced melt, along with peritectic garnet and cordierite, starting at ~0.5 to 0.6 GPa (18- to 22-km depth, assuming a crustal density of 2.8 g/cm^3), 720° to 730°C (*4*). Further decompression to ~0.35 GPa (exhumation to ~13-km depth), 700° to 730°C, led to additional

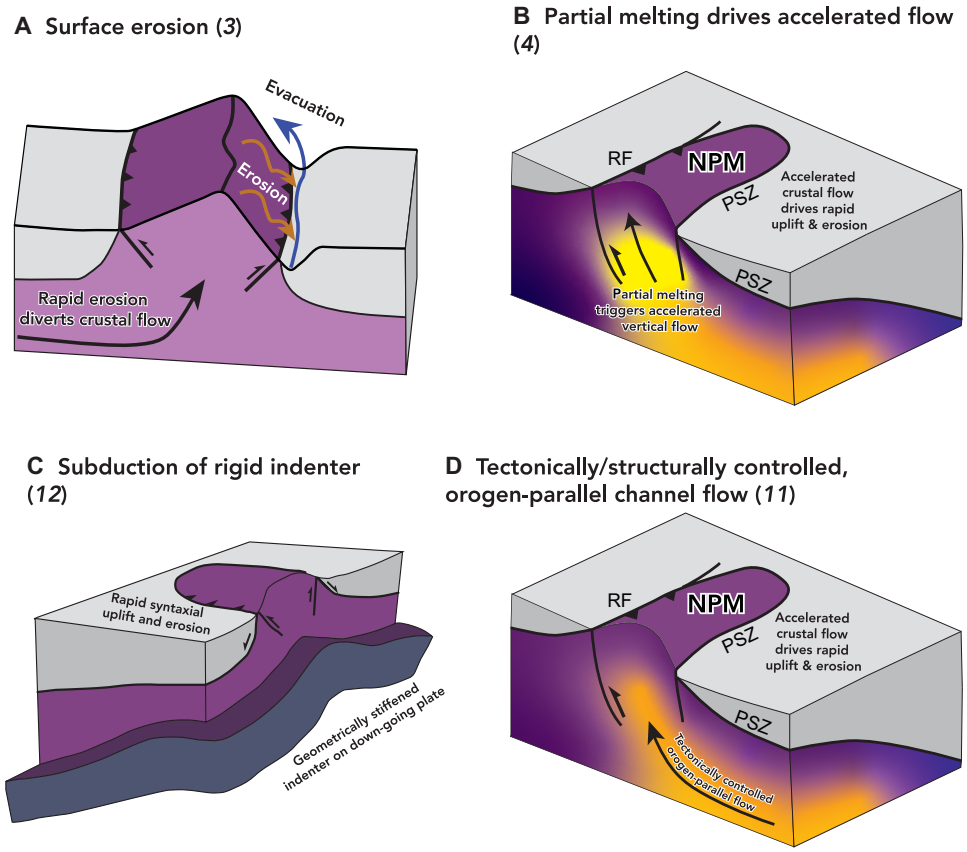

Fig. 2. Schematic cartoons of proposed end-member driving mechanisms for ultrafast exhumation in the Himalayan syntaxes from (*3*, *4*, *11*, *12*). (**A**) Modified after (*3*) with permission from Geological Society of America. (**B**) Modified after (*71*), with structures from (*66*). (**C** and **D**) Modified after (*12*) with structures from (*66*). (B to D) Modified and reused with permission from American Geophysical Union.

cordierite growth, garnet resorption, and melt crystallization (*4*). We recalculated previously published phase equilibria for this sample, testing the sensitivity of the inferred *P-T* path, and the pressures and temperatures of the melting and crystallization reactions discussed above, to input parameters such as the specific thermodynamic data and bulk-rock MnO content, obtaining similar results in all cases (fig. S4). Final melt crystallization occurred at 0.25 to 0.35 GPa (~9- to 13-km depth) at 0.988 ± 0.003 Ma, based on high-precision isotope dilution thermal ionization mass spectrometry (ID-TIMS) $^{207}Pb/^{235}U$ dates from oscillatory-zoned xenotime (*4*), implying a time-averaged exhumation rate of 9 to 13 mm/year for the past ~1 Ma (Fig. 4B and fig. S4).

Monazite grains in K-94-29 generally exhibit resorbed, low-Y, high-Th cores surrounded by higher-Y, lower-Th rims. Some grains exhibit multistage overgrowths marked by sharp changes in trace element content, with successive domains exhibiting progressively higher Y and lower Th. Monazite grains are found as inclusions in cordierite patches surrounding garnet and in plagioclase, K-feldspar, and quartz (Fig. 4C and fig. S5). Some grains exhibit zoning indicative of multistage growth, with decreasing Th and increasing Y with each successive growth zone outward from the grain core (Fig. 4C and fig. S5).

Monazite petrochronology

In K-94-30, fifty-eight laser-ablation split-stream (see Materials and Methods) spot analyses from eighteen monazite grains were performed. Six analyses yield large date uncertainties (>1.0 Ma) and anomalously low $^{208}Pb/^{204}Pb$ ratios and are not considered further in our interpretations. Common Pb–corrected $^{208}Pb/^{232}Th$ dates from the fifty-two remaining analyses range from 2.9 ± 0.6 Ma to 0.9 ± 0.2 Ma (data S1). In K-94-29, thirty-two spot analyses from nine monazite grains (see Materials and Methods) were performed. Eleven analyses yielded large date uncertainties (>1.0 Ma) and are excluded from further consideration. Of the remaining nineteen analyses, most give common Pb–corrected $^{208}Pb/^{232}Th$ dates ranging from 4.1 ± 0.5 Ma to 1.5 ± 0.1 Ma, with two older dates at 5.7 ± 0.4 Ma and 7.1 ± 0.2 Ma (data S2). In both samples, the trace element composition of monazite varies systematically with monazite spot date (see Supplementary Text and figs. S6 and S7). To constrain the petrologic processes responsible for temporal variations in monazite chemistry, we reduced the dimensionality of the monazite age and trace element dataset with a principal components analysis (PCA; Fig. 5), which we discuss below. Details of the statistical methods used are presented in Materials and Methods.

In both samples, the PCA revealed two principal components that collectively explain ~90% of the total variance of the dataset. The dominant principal component, X_1, accounts for ~83% of the total variance in K-94-30 and ~69% of the total variance of monazite composition in K-94-29. Factor loadings of the chondrite-normalized rare earth element (REE) concentrations for X_1 show that monazite analyses with positive X_1 scores are correlated with higher Y + medium and heavy REE (M-HREE) concentrations, whereas analyses

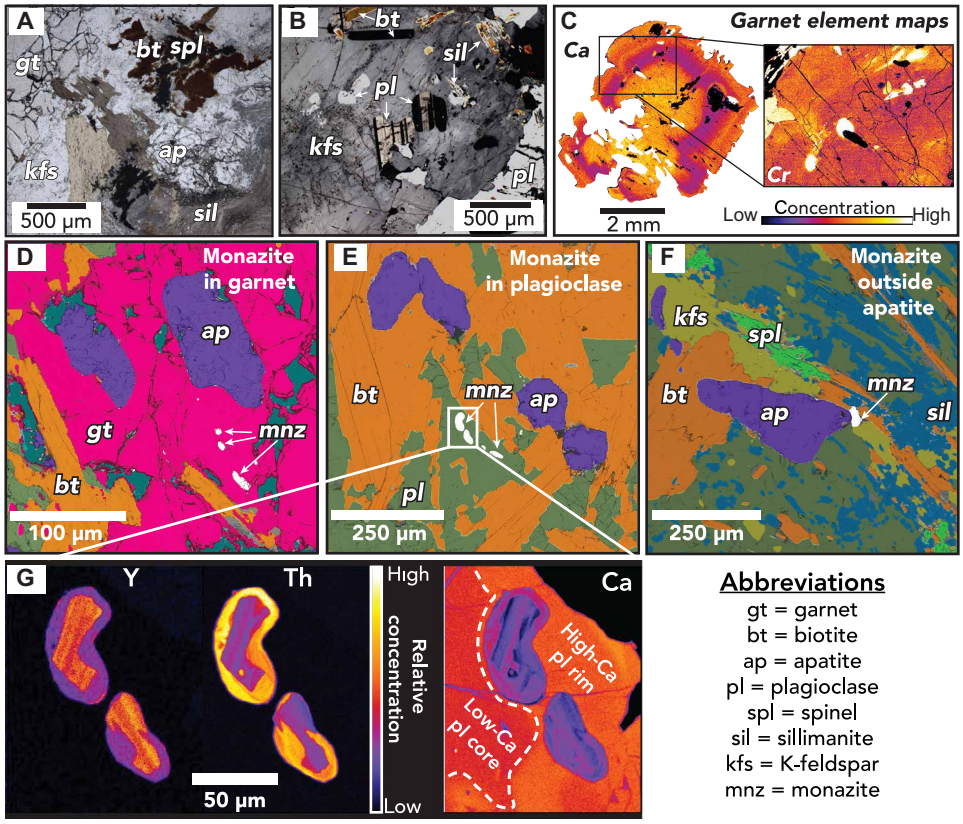

Fig. 3. Mineral textures of sample K-94-30. (**A** and **B**) Plane polarized light photomicrographs of mineral textures showing evidence of biotite breakdown melting. (**C**) X-ray maps of garnet showing the distribution of Ca and Cr in garnet. Inset for the Cr map is indicated in the Ca map. (**D** to **F**) Phase maps showing microstructural locations of monazite. (**G**) X-ray maps of Y, Th, and Ca zonation in monazite.

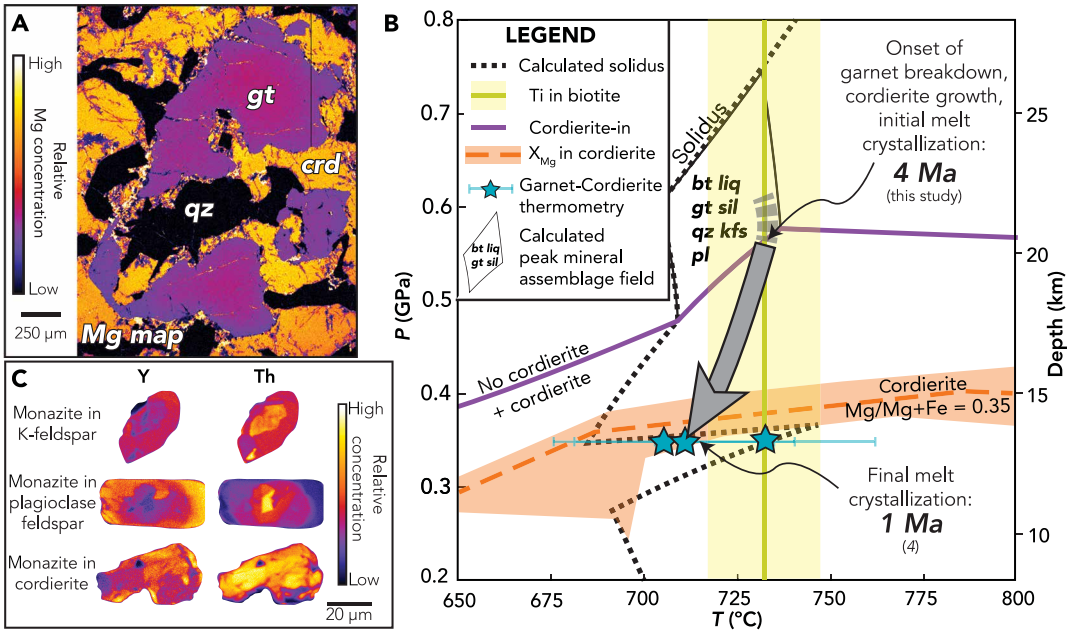

Fig. 4. Mineral textures and *P-T-t* history of sample K-94-29. (**A**) Mg x-ray map of resorbed garnet (gt) replaced by cordierite (crd) and quartz (qz). (**B**) Pressure-temperature plot showing the summary of thermobarometric and petrochronologic constraints for sample K-94-29 from both (*4*) and this study. (**C**) X-ray maps of Y and Th for selected monazite grains from different textural settings.

with negative X_1 scores are correlated with lower Y + M-HREE concentrations (Fig. 5, A and B, and fig. S8). These elemental groupings likely describe a dominant influence of garnet on the Y + M-HREE concentrations during monazite growth (*19*). In K-94-30, lower X_1 scores are correlated with lower Eu concentrations, and Eu/Eu* is not correlated with Sr (figs. S6 and S8); these patterns likely reflect the influence of K-feldspar on X_1 in K-94-30 such that lower X_1 scores (and thus lower Eu concentrations) indicate monazite crystallization

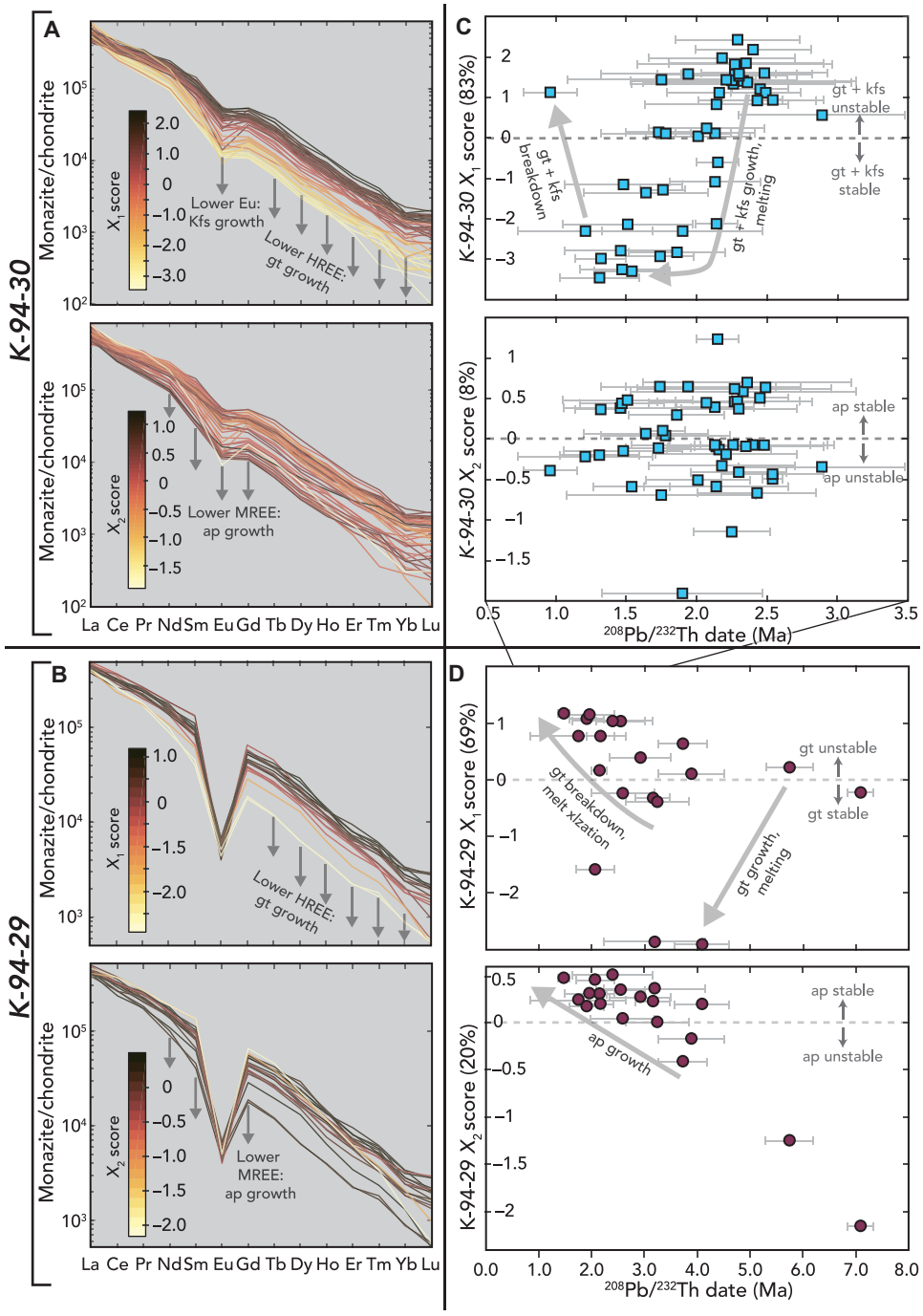

Fig. 5. Results of monazite petrochronology and principal components analysis. (**A**) Chondrite-normalized rare earth element plot showing trace element variation of monazite in sample K-94-30, with each analysis color-shaded according to its principal component (X_1 and X_2) scores. (**B**) The same as in (A) for sample K-94-29. (**C**) Plot of ^{208}Pb/^{232}Th date versus principal component (X_1 and X_2) scores for sample K-94-30. Horizontal dashed line indicates where principal component scores equal zero. Gray arrows illuminate temporal trends in principal component scores, with gray text showing our interpretations. 2σ error bars for ^{208}Pb/^{232}Th date are shown for each analysis in each plot. (**D**) Same as in (C) for sample K-94-29. Mineral abbreviations are the same as in Figs. 2 and 3. Lines emanating from Panel D show correspondence with ^{208}Pb/^{232}Th date range for sample K-94-30 in (C).

during K-feldspar growth (*19*). This is not the case for K-94-29, for which Eu does not influence X_1 (i.e., loading factors are close to zero; fig. S8).

The second principal component, X_2, accounts for ~8% of the total variance in K-94-30 and ~20% in K-94-29. Monazite with high X_2 scores is associated with MREE depletion; lower X_2 scores are associated with MREE enrichment (Fig. 5, A and B, and fig. S8). These patterns likely show the dominant influence of apatite on X_2 such that negative X_2 scores correspond to monazite crystallization during apatite breakdown; positive scores correspond to monazite crystallization during apatite growth (*20*).

The dominant principal components identified indicate similar petrogenetic controls on the composition of monazite in both samples (growth and breakdown of garnet ± K-feldspar and apatite). However, those processes appear to have occurred at different times. In K-94-30, X_1 scores have similar positive values (~1 and 2) between 2.5 and 2.2 Ma, indicating garnet breakdown at this time (Fig. 5C). After 2.2 Ma, analyses show negative X_1 scores, implying garnet and K-feldspar growth, which trend toward progressively lower values through time and reach a minimum value of −3.5 at 1.3 Ma (Fig. 5C). Thus, monazite likely records garnet and K-feldspar growth between 2.2 and 1.3 Ma, coincident with an increase in monazite Th concentration (fig. S6). Analyses younger than 1.3 Ma have higher X_1 scores, with the youngest analysis of 0.9 Ma having a positive X_1 score (1.1), suggestive of garnet ± K-feldspar breakdown at this time. X_2 scores for K-94-30 show no systematic variation with age, with scores showing both positive and negative values throughout the range of $^{208}Pb/^{232}Th$ dates (Fig. 5C).

In K-94-29, the two oldest spot analyses show X_1 scores around 0. The analysis with the lowest X_1 score has a $^{208}Pb/^{232}Th$ date of 4.1 Ma, suggestive of garnet growth at this time. X_1 scores are positive from 3.9 Ma and show a general increase with progressively younger spot dates (Fig. 5D), consistent with progressive garnet breakdown between 4.1 and 1.5 Ma. This trend is coincident with decreasing Th starting at ~4 Ma (fig. S7). X_2 shows positive scores beginning at 4.1 Ma, also generally increasing with progressively younger analyses (Fig. 5D), reflecting progressive apatite growth during this interval.

DISCUSSION

Petrologic evolution: K-94-30 (restitic pelite)

The trace element compositions, internal textures, and textural settings of the dated monazite grains allow us to interpret isotopic dates in the context of the petrologic and *P-T* evolution of the samples. Although we cannot exclude the influence of unmapped structures within the massif that may separate the original outcrops of the samples, we emphasize that the sampling localities of these rocks and the lack of known internal structures within the massif are both consistent with our assumption that each sample experienced a common *P-T-t* history. The temporal trends in monazite chemistry allow us to reconstruct their divergent reaction histories throughout this *P-T-t* history.

In K-94-30, we interpret the cluster of analyses with dates of ~2.5 to 2.2 Ma and high X_1 scores (corresponding to high Y, low-Th monazite cores) to record the growth of high-Y monazite cores during garnet and apatite recrystallization. This is consistent with expected Y + M-HREE partitioning from Pyle *et al.* (*21*) in a prograde reaction in which Y-rich garnet reacts with apatite to produce Ca-rich garnet, Ca-rich plagioclase feldspar, and Y-rich monazite. This interpretation draws support from textural observations of monazite growing in close proximity to resorbed apatite and low-Ca plagioclase cores, and inclusion of monazite in high-Ca plagioclase rims (Fig. 3). From 2.2 to 1.3 Ma, decreasing X_1 scores (corresponding to low-Y, high-Th monazite overgrowths) and increasing Th (fig. S6) are interpreted to record monazite (re)crystallization during peritectic garnet and K-feldspar growth and partial melting, consistent with textures indicative of biotite breakdown melting (Fig. 3). The negative correlation of Th and total REE concentrations (fig. S6) is consistent with elemental exchange between monazite and silicate melt (*22*). The data therefore suggest a period of biotite breakdown melting between 2.2 and 1.3 Ma, in which peritectic K-feldspar and high-Ca and Cr garnet rims grew. This brief duration of garnet growth is consistent with the preservation of original, prograde chemical zonation in the cores of millimeter-sized garnet (*17*). The youngest datum of 0.9 Ma suggests a return to high Y, low Th, and Sr concentrations, and positive X_1 scores by 0.9 Ma, recording monazite growth during garnet breakdown and melt crystallization—consistent with the thin, outermost high-Y rims observed on some monazite grains (Figs. 3 and 5).

In summary, we interpret monazite in K-94-30 to record the following petrologic evolution: (i) Between ~2.5 and 2.2 Ma, partial garnet and apatite breakdown resulted in the initial growth of high-Y monazite cores and high-Ca garnet and plagioclase rims; (ii) between 2.2 and 1.3 Ma, partial melting, K-feldspar growth, and continued growth of high Ca garnet rims were accompanied by the development of low-Y monazite rims; (iii) melt crystallization and garnet breakdown were underway by 0.9 Ma (Fig. 5C).

Petrologic evolution: K-94-29 (migmatitic orthogneiss)

In K-94-29, a drop in X_1 scores (lower Y + HREE) and a concomitant increase in Th (Fig. 5D and fig. S7) between 5.7 and 4.1 Ma are interpreted to record monazite (re)crystallization during biotite breakdown melting, involving garnet growth and feldspar decomposition. According to phase equilibria calculations (fig. S4) (*4*), such partial melting occurred as the rock decompressed through 0.5 to 0.6 GPa at 720° to 730°C. The progressive enrichment in Y and HREE in monazite beginning ~4 Ma is interpreted to record monazite crystallization during subsequent garnet breakdown. This is confirmed by the increasing X_1 scores after 4.1 Ma, with analyses yielding positive X_1 scores after 3.9 Ma (Fig. 5D). A concomitant decrease in Th in monazite is consistent with growth during progressive melt crystallization and fractionation of Th from the melt by monazite (*23*). Decreasing Sr and Eu/Eu* in monazite through this time interval are interpreted to track coeval feldspar growth (*24*). The positive and increasing X_2 scores through this time interval suggest coeval apatite growth. The temporal trends in monazite chemistry in K-94-29 are consistent with the textural settings of monazite (occurring as inclusions in cordierite, quartz, and feldspar) as well as the internal chemical zonation in some monazite grains, which indicate multistage growth of increasingly higher-Y and lower-Th monazite (Fig. 4C).

In summary, we interpret monazite in K-94-29 to record (i) biotite breakdown melting beginning sometime between 5.7 and 4.1 Ma and (ii) progressive garnet breakdown, cordierite growth, and melt crystallization from ~4 to 1.5 Ma (Fig. 5D). Previous high-precision ID-TIMS xenotime dates from this sample from Crowley *et al.* (*4*) suggest that melt crystallization was probably complete by 0.99 Ma.

Melting, crystallization, and exhumation histories

Our petrochronologic analysis shows that Plio-Pleistocene partial melting in the core of the NPM was not synchronous in the two samples considered: Progressive crystallization of melt produced by biotite breakdown melting in sample K-94-29 occurred during exhumation, which began between 5.7 and 4.1 Ma, before the onset of biotite breakdown melting in K-94-30, which began ~2.2 Ma and continued to ~1.3 Ma. In situ melt crystallization in K-94-29 began at ~4 Ma and was nearly finished at 0.99 Ma, at which point melt crystallization in K-94-30 had likely only begun. The observed disparate timing of melting can be explained by likely prior melt loss that led to the restitic (muscovite and quartz-free) mineral assemblage observed in K-94-30. Because of positive Clapeyron slopes of biotite breakdown melting reactions (*15*), this would result in crossing of the biotite breakdown melting reaction at lower pressures during near isothermal decompression than in more fertile rocks.

The data presented here, in combination with previous geochronology and *P-T* constraints on the onset and termination of garnet breakdown, cordierite growth, and melt crystallization in K-94-29 from (*4*), allow us to reconstruct the time-averaged Plio-Pleistocene exhumation rates of the NPM. Garnet breakdown, cordierite growth, and melt crystallization began ~4 Ma at depths of 18-22 km (assuming a crustal density of 2.8 g/cm^3). Final melt crystallization occurred by 0.99 Ma at 9- to 13-km depth, indicated by the coincidence between the predicted composition of cordierite rims and crossing of the *P-T* path through the solidus (*4*). Collectively, these data suggest that exhumation from depths of 18-22 km to 9-13 km (i.e., 5 to 13 km of total exhumation) occurred over a duration of ~3 Ma, resulting in time-averaged exhumation rates of ~2 to 4 mm/year before 0.99 Ma. Since at least 0.99 Ma, exhumation rates have been 9 to 13 mm/year—similar to estimates of modern surface denudation rates in the NPM (*25*). This implies that exhumation accelerated considerably ~1 Ma.

The validity of our interpretations can be tested by assessing the magnitudes of potential sources of uncertainty in our data and their effects on the inferred exhumation rates. The petrologically derived exhumation rates calculated here require precise quantification of (i) the pressure (depth) at which replacement of garnet by cordierite began in K-94-29, (ii) the pressure at which final equilibration and melt crystallization occurred, and (iii) the timing of these petrologic events. The pressures at which reactions occurred are constrained by phase equilibria modeling calculations, for which uncertainties arise from the thermodynamic data, activity-composition models, and bulk composition used for modeling. The uncertainties associated with phase equilibria modeling are difficult to quantify precisely, although maximum uncertainties on pressure on any calculation are considered to be ±0.1 GPa (*26*). The modeling presented in (*4*) used thermodynamic data and activity-composition models that have since been updated. It also excluded MnO from the bulk-rock composition, which has the effect of potentially reducing the apparent stability of garnet at lower pressures, thus affecting the interpreted exhumation history. Our calculations, which incorporate MnO and up-to-date activity-composition models, show that the range of pressures deduced for key reactions varies by ±0.05 GPa when considering different combinations of thermodynamic data and activity-composition models, as well as subtly different bulk-rock MnO contents (fig. S4). However, the total interpreted pressure difference between initial and final cordierite growth and melt crystallization is nearly identical regardless of the thermodynamic data and activity-composition models used, or amount of MnO in the bulk-rock composition.

The timing of final melt crystallization is well constrained, with the youngest oscillatory-zoned xenotime in (*4*) giving a precise date of 0.988 ± 0.003 Ma. The timing of initial cordierite growth and garnet resorption is less well constrained, although our monazite data place a minimum bound of 4.1 ± 0.5 Ma, as analyses younger than this give progressively increasing and dominantly positive X_1 scores, indicating monazite growth during garnet breakdown. Propagation of uncertainties on the bounding dates and pressures (assuming 0.1 GPa uncertainty and crustal density of 2.8 kg/m^3) yields a decompression rate of 0.06 ± 0.04 GPa/Ma, or a 2.3 ± 1.7 mm/year exhumation rate, between 4.1 and 0.99 Ma. According to this analysis, the maximum time-averaged exhumation rate during this time span is 4 mm/year. If the timing of initial cordierite growth and garnet resorption is older than 4.1 Ma, exhumation rates during this period would be lower. Between 1 and 0 Ma, our analysis indicates that the minimum time-averaged exhumation rate was 9 mm/year. We therefore interpret our data to record a substantial acceleration in exhumation of the NPM at around 1 Ma, from 2 to 4 mm/year to 9 to 13 mm/year. A similar acceleration was hypothesized in (*4*) to have begun 1.7 Ma, but the lack of textural and chemical context of dated mineral grains prevented their ability to link isotopic dates to metamorphic reactions and thus resolve the exact timing of the acceleration. Our data confirm their hypothesis and better constrain both the timing of accelerated exhumation and the rates of exhumation before the onset of ultrafast exhumation.

Modern exhumation rates throughout the rest of the Himalaya have been estimated by low-temperature thermochronologic studies (*27*, *28*); however, the depths and time scales over which these techniques can quantify exhumation rates (and any changes thereof) are limited by the elevated near-surface thermal gradient in the NPM (>100°C/km) (*29*, *30*). Therefore, the exhumation rates—and any changes in exhumation rate—when rocks of the NPM were still >700°C may be most robustly constrained by linking the timing and *P-T* conditions of high-temperature metamorphic mineral growth, as demonstrated here.

Constraints on NPM exhumation from thermal modeling

A simple thermal model was constructed to examine whether the petrologically constrained *P-T-t* path discussed above is consistent with exhumation at various rates and to investigate the permissible geologic conditions necessary to reproduce the *P-T-t* path. For simplicity, we modeled a 1D, 22-km-thick vertical column, assuming a constant basal temperature of 750°C, intended to simulate a constant flow of migmatitic rock in the middle crust beneath the NPM. This geometric simplicity can be justified by the high exhumation rates at Nanga Parbat, which yield Peclet numbers > 1 (Pe = Lu/α, where L is the characteristic length scale, u is the flow velocity, and α is the thermal diffusivity) for plausible parameter ranges and imply an advection-dominated thermal field (e.g., Pe ~2 or ~5 for 5 mm/year flow velocity, 1×10^{-6} m^2/s thermal diffusivity, and 10- or 30-km length scale, respectively; Pe ~3 or ~10 for the same conditions but at 10 mm/year flow). The thermal effects of horizontal or shallowly inclined flow were not considered and potentially limit the applicability of our model, although we note that the deep crustal velocity field below Nanga Parbat is currently poorly known. In the absence of such constraints, we assumed that any subhorizontal crustal flow delivers hot, partially molten crust to the base of a steeply exhuming

column, maintaining a constant temperature at 22-km depth. Radiogenic heat production was set to 3 μW/m^3 throughout the column, consistent with high U and Th contents of NPM gneisses (*31*).

We considered various combinations of exhumation rate over the past 10 Ma, with exhumation at or below 2 mm/year yielding *P-T* paths much cooler than the petrologic constraints (solid and dotted gray curves in Fig. 6). Exhumation at a constant 5 mm/year (the time-averaged exhumation rate derived from our data) produces a *P-T* path that is characterized by similar isobaric decompression to the petrologic constraints but would result in samples that were at least 5 km shallower and 200°C cooler than our results by 1 Ma (dashed gray curve; Fig. 6)—far outside the bounds of thermobarometric uncertainties. Models that simulate 10-mm/year exhumation since 1 Ma and 2 to 4 mm/year in the interval between 4 and 1 Ma are generally too cold if exhumation either began 4 Ma or was slow before that (green curves in Fig. 6). It thus appears that the onset of exhumation at rates ≥5 mm/year predated 4 Ma.

Models that simulate 5 mm/year exhumation between 10 and 4 Ma (i.e., before our samples arrived at the base of the modeled column) result in early heating of the crustal column at shallower depths and can produce *P-T-t* paths that broadly agree with petrologic and geochronologic constraints from this study and in (*4*). In these cases, we explored a range of exhumation rates after 4 Ma, with all experiencing at least 10 mm/year exhumation in the past 1 Ma (yellow curves in Fig. 6). Although it is difficult to assess the relative merits of each of these models (given the uncertainty on petrologic and geochronologic constraints and the simplicity of the 1D model), it is clear that a simulation for exhumation rates estimated directly from the available constraints (13 mm/year since 1 Ma and 2 to 4 mm/year before then) produces a reasonable fit to the petrologically constrained *P-T*-t path (blue curve; Fig. 6). All model results also show reasonable agreement to geologically constrained estimates of the modern near-surface geothermal gradient in the core of the NPM (>100°C/km) (*29*), although our 1D thermal model is too simple to accurately model thermal gradients in mountain belts in which topography may strongly influence isothermal structure.

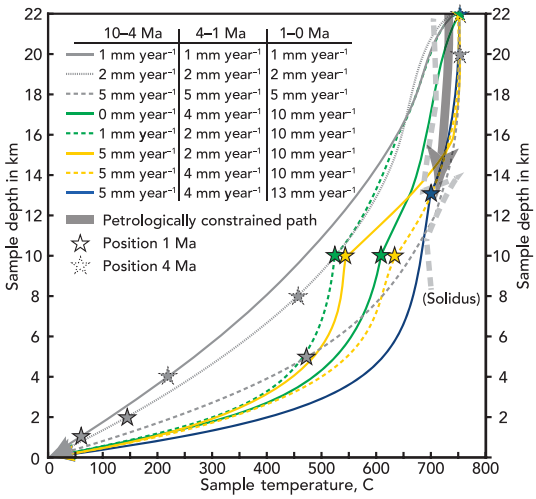

Fig. 6. Results of 1D thermal model. *P-T-t* paths calculated for various combinations of exhumation rates, assuming a constant temperature of 750°C at 22-km depth (gray, green, yellow, and blue curves). Legend panel identifies the exhumation rate at 10 to 4 Ma, 4 to 1 Ma, and after 1 Ma for each curve. Large gray arrow and light gray dashed curve represent petrologic constraints on the *P-T* path and the position of the solidus, respectively (both as in Fig. 4B).

Our modeling suggests that continual, rapid (5 mm/year) extrusion of hot (~750°C) crust from 22-km depth in the NPM starting at ~10 Ma advected heat and deflected crustal isotherms toward the surface (*29*, *32*). This elevated the near-surface thermal gradient and produced near-isothermal conditions in the middle crust before 4 Ma, required by the *P-T-t* path of our samples. High near-surface geothermal gradients before 4 Ma could be achieved by other mechanisms not explored by our thermal model, such as increased basal heat flow from the mantle or continuous melt migration and emplacement at shallow depths before ~4 Ma (*33*). There is no evidence for thermal erosion of the lithospheric mantle beneath the NPM (*34*), discounting the role of increased mantle heat flow. Although leucogranite intrusions in the NPM have been emplaced from Miocene to Pleistocene time (discussed below), the relative volume of leucogranite in the NPM is thought to be minor (Fig. 1), and the solidus temperatures of leucogranite intrusions were not higher than the peak temperatures of the rocks in which they were emplaced. Therefore, melt migration likely did not exert a dominant control on the heat budget of the NPM during exhumation. These observations, in concert with our thermal modeling, suggest that our petrochronologic results require antecedent flow of hot middle crust into, and extrusion out of, the NPM. The same process has been proposed to occur in the eastern Himalayan Syntaxis based on magnetotelluric imaging of the lower crust beneath the NBM (*35*). Below, we discuss potential roles of different exhumation mechanisms that could have driven the pulse of rapid exhumation in the NPM recorded by our samples.

A modern pulse of ultrafast syntaxial exhumation

The total, time-averaged exhumation rate implied by our data is between 4.5 and 5.5 mm/year, consistent with previous long-term estimations of exhumation rates in the NPM since the Miocene (*5*, *9*). However, we show here that exhumation in the NPM may be pulsed, with periods of slower, but still rapid exhumation (~2 to 4 mm/year) punctuated by a phase of ultrafast exhumation (9 to 13 mm/year) in the past 1 Ma. Petrologic studies suggest that the former midcrustal channel preserved in the exposed Greater Himalayan Sequence in the central Himalaya (Fig. 1) underwent brief periods of anomalously rapid exhumation approaching plate tectonic rates (6 to 10 mm/year) in Oligo-Miocene time, themselves thought to represent pulses of accelerated midcrustal flow (*36*–*38*). The syntaxial massifs of the orogen are currently the sites of the highest intracontinental exhumation rates on the modern Earth. However, our data reveal that ultrafast exhumation in the NPM has only operated for ~1 Ma and was preceded by several million years of slower exhumation (Figs. 6 and 7). Recent studies have documented a similar acceleration of exhumation to ultrafast rates (from ~1 to 4 mm/year to 9 to 10 mm/year) in the eastern Himalayan syntaxis—the NBM, which also began ~1 Ma (Fig. 7) (*12*, *13*). Thus, the ultrafast exhumation rates observed in both syntaxial massifs are a geologically recent phenomenon and may represent a modern exhumation "pulse" against a background of slower, but still anomalously rapid, exhumation rates (Fig. 7). The synchroneity of this pulse in both syntaxes—but not in Greater Himalayan Sequence in the central Himalaya (Fig. 7)—implies that a common process was responsible for localized accelerated exhumation in the syntaxes; below, we discuss possible geodynamic mechanisms for this acceleration (Fig. 2).

Onset of ultrafast exhumation: The role of surficial processes

A current paradigm for the initiation of rapid exhumation in the syntaxial massifs is the Tectonic Aneurysm model, in which spatially focused surface denudation driven by the Indus River locally accelerates rock uplift and exhumation of hot mid and lower crust at the syntaxes (*3*, *32*). The Indus River likely formed ~40 Ma when the Tibetan plateau rose to near its present height (*39*). It was definitely set in course before 20 Ma, when the dextral strike-slip Karakoram fault diverted it by ~120 km (*40*, *41*). The Indus River cuts diagonally across the north-south (N-S) trending NPM before turning south along the western margin of NPM roughly coincident with the Rakhiot fault (Fig. 1B). Our data do not specifically address the role of the Indus River in driving initial exhumation of the NPM, which is thought to have begun ~10 to 13 Ma (*42*, *43*). However, the antecedence of the Indus River relative to the Pleistocene acceleration in exhumation, as well as evidence for a stable drainage configuration (i.e., no major stream capture events) in the western Himalaya since the late Miocene (*44*) preclude the role of fluvial erosion in triggering accelerated exhumation at ~1 Ma.

Glacial erosion has also been postulated to cause intense localized erosion, crustal deformation, and uplift during orogenesis (*45*, *46*). The ~1-Ma acceleration in exhumation coincides with the mid-Pleistocene transition, a period between 1.2 and 0.7 Ma in which the duration of glacial-interglacial cycles increased from 41 to 100 ka. The effect of longer glacial cycles could enhance the efficacy of glaciers as agents of surface erosion (*45*). Glacial erosivity is expected to scale with glacier mass (*47*); thus, longer glacial-interglacial cycles allow glaciers to build greater mass and hence erode more. Enhanced erosivity of glaciers as a result of the mid-Pleistocene transition has been suggested to locally accelerate exhumation in glaciated areas where rapid, tectonically driven exhumation is already occurring (*45*, *48*). Models suggest that enhanced surface heat flux in tectonically active regions may promote development of warm-based glaciers and thus induce more effective, localized glacial erosion in areas where the near-surface thermal gradient, dictated by tectonic processes, is high (*49*). The NPM has an enhanced near-surface geothermal gradient due to upward bowing of isotherms in the core of the massif, driven by antecedent upward flow of hot middle crust (*29*, *30*). Thus, the NPM may have been primed for rapid exhumation by increased glacial erosion at the mid-Pleistocene transition.

Despite this, several observations suggest that glacial erosion was not solely responsible for the acceleration in exhumation and rock uplift. First, the high-surface topography of the NPM compared to its surroundings shows that erosion rates have not kept pace with rock uplift over at least the past 1 Ma. The N-S trend and antiformal nature of the massif is opposite to the arcuate, mainly east-west (E-W) trend of high-glacial coverage along the Himalaya, and the highest rates of exhumation are observed in the southern part of the NPM, around the core zone of the highest-grade metamorphic rocks. If glacial erosion exerted the primary control on the location of rapid exhumation of midcrustal rocks in the massif, we expect the massif to have a dominantly E-W trend, and/or exhumation rates to be similarly high in the northern part of the massif, which is also glaciated. Furthermore, the adjacent Karakoram range, which has a uniformly greater glacial coverage (and thus likely more glacial erosion potential) than the NPM (*50*), has not undergone uniformly extreme rates of mid-Pleistocene exhumation (*51*). Last, the NBM in the eastern syntaxis appears to have undergone a similar acceleration in exhumation rates ~1 Ma (*7*, *8*, *52*), in a much wetter climate, in which we would expect more effective glacial erosion.

These observations suggest that surface processes and tectonic uplift may engage in a positive feedback at the syntaxes, but that surface erosion responds to rock uplift rather than vice versa, at least over the 10^5 to 10^6 Ma time scales considered here. The accelerated exhumation at ~1 Ma must therefore be primarily driven from the bottom-up as a manifestation of (i) a change in the rheology of the Himalayan middle crust driven by, for example, an episode of partial melting, (ii) a structurally dictated change in mass flux in the syntaxes, (iii) a change in tectonic forcing or plate geometry that increased mass flux to and in the syntaxes, or (iv) a combination of these processes. We discuss below the plausibility of these processes in the context of the new petrochronologic data presented here.

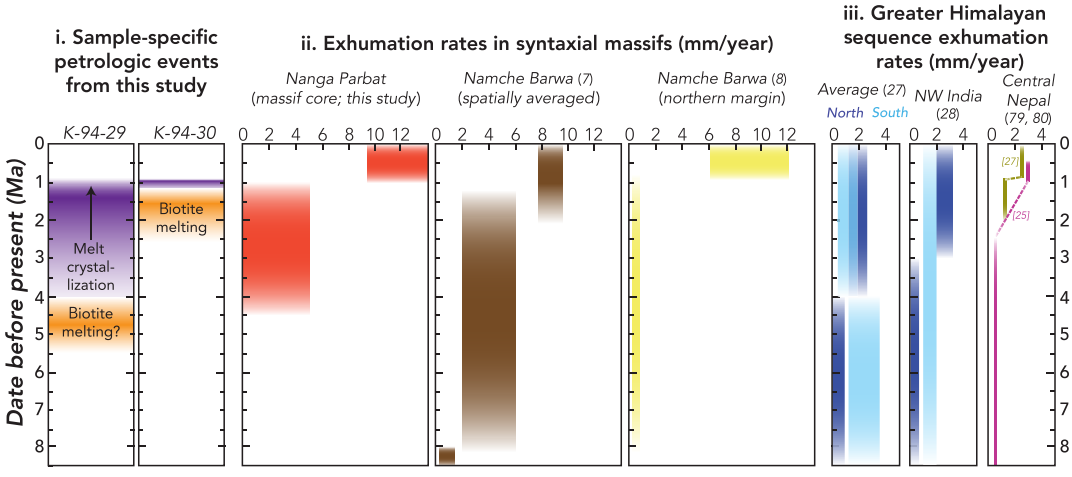

Fig. 7. Temporal correlation of study results to previous work. This compilation illuminates relationships between the timing of (from left to right) (i) different petrologic events in the studied samples; (ii) magnitudes of changes in exhumation rates in Nanga Parbat (based on our data) and Namche Barwa, based on data from (*7*) and (*8*); and (iii) magnitudes of, and changes in, exhumation rates in the Greater Himalayan Sequence from other parts of the Himalaya (*27*, *28*, *79*, *80*).

Onset of ultrafast exhumation: The role of crustal weakening and buoyancy upon melting

Partial melting, even to small extents of just a few volume percent melt, can decrease rock strength by at least one order of magnitude (*53*). Thus, partial melting and associated crustal weakening may trigger and/or accelerate ductile midcrustal flow and rapid exhumation in active orogenic belts. Moreover, the buoyancy increase associated with partial melting may assist exhumation (*54*). Oligo-Miocene pulses of rapid exhumation in the Greater Himalayan Sequence are thought to have been triggered by partial melting that occurred just before, or coeval with, the period of rapid exhumation (*36*–*38*, *55*). This was suggested to explain ultrafast exhumation in the NPM in (*4*), which proposed that the biotite breakdown melting reaction, crossed during decompression through ~0.5 GPa, sufficiently weakened the crust to trigger the onset of extremely rapid exhumation. However, we show that the onset of biotite breakdown melting in the studied samples (~4 Ma in K-94-29 and ~2.1 Ma in K-94-30) and the acceleration of their exhumation (1 Ma) were diachronous: In situ melt crystallization in some rocks may have been complete, while others may have been melting at the onset of accelerated exhumation (Fig. 7). This makes it difficult to conclusively attribute bulk crustal weakening in the NPM core due to in situ, late-stage biotite breakdown melting as the dominant trigger for its exhumation at extreme rates.

Could an episode of partial melting at deeper crustal levels have weakened an already-deforming and flowing crust sufficiently to accelerate crustal flow and exhumation at ~1 Ma? Throughout the entire span of monazite dates recorded here (7.1 to 0.9 Ma), granitic magmas were being emplaced into the rocks now exposed in the core of the NPM, crystallizing into tourmaline leucogranites (*4*–*6*, *42*, *56*). Rb-Sr isotopic analysis of these leucogranite bodies shows that they were derived from muscovite breakdown melting of rocks at greater depth than the current exposure (*15*). Thermodynamic modeling suggests that fertile lithologies (e.g., water-saturated metapelites) may produce 4 to 5 mole percent (mol %) melt through muscovite breakdown melting upon reaching 730°C (*57*): sufficient to substantially weaken the crust (*53*) but not enough to induce buoyancy-driven diapiric flow (*54*). Several leucogranite bodies were emplaced/crystallized just before the onset of and during the accelerated exhumation shown here. These include the 1.4-Ma Mazeno Pass pluton, the 1.8- to 1.1-Ma Rupal dikes, and 0.7-Ma dikes in the outer margins of the massif (*4*–*6*, *42*, *56*). Seismic and magnetotelluric studies suggest the presence of water-undersaturated middle and lower crust under the NPM and the absence of large connected volumes of melt (*58*).

Muscovite breakdown melting at depth was clearly occurring near the onset of accelerated exhumation in the NPM and is likely ongoing today, but whether such melting was sufficiently voluminous and occurred episodically to trigger accelerated exhumation is unknown. The synchroneity in accelerated exhumation in both syntaxes suggests a common driving mechanism for ultrafast exhumation. Thus, if attainment of some critical melt fraction was essential to trigger a pulse of exhumation in the syntaxes, a pulse of abundant leucogranite generation at ~1 Ma should also be seen in the NBM. While zircon rims in granitic glacial float from the NBM as young as ~1 Ma have been dated, the volumes of such granites and the petrological significance of such dates are unknown (*59*). Existing petrochronology of migmatites from the NBM does not show evidence of Pleistocene metamorphism and melting (*60*–*62*). Further mapping, geochronology, and quantification of leucogranite volumes in both syntaxes and constraints on the modal abundance of muscovite in the source rocks for these melts (*15*) are necessary. Regardless, a synchronous partial melting "event" would require the crust beneath both syntaxes to have similar melt fertility (governed by the distribution of melting reactants, fluid availability, and melt loss history during previous episodes of metamorphism) and thermal histories—a seemingly unlikely coincidence (*63*).

Onset of ultrafast exhumation: The role of structural control and tectonic forcing

Rock uplift in the NPM is accommodated by active faults/shear zones on its eastern and western margins that accommodate E-W contraction indicated by field and geodetic studies (Fig. 1) (*63*–*67*): a west-vergent thrust fault on the west (Rakhiot-Liachar thrust) and a steeply dipping east-side down fault on the east (Stak fault). The Stak fault has not been studied in detail; modern slip rates are unknown, although neotectonic displacement is thought to be relatively minor (Fig. 1C) (*64*, *66*). Geodetic studies reveal dominantly westward movement of the NPM (relative to the adjacent Kohistan terrane) and an asymmetric present-day velocity field, with the highest velocities recorded on the western margin of the massif (*65*, *67*). This suggests that the Rakhiot-Liachar thrust, which slips between 5 and 20 mm/year (*65*, *67*), combined with distributed deformation in the core of the massif (*68*), is responsible for active uplift of the NPM (Fig. 1) and enables exhumation of hot middle crust (*66*, *69*). Although ambiguity remains regarding which structures of the NPM played a role in its exhumation and at what points in its evolution different structures were active (*63*), existing constraints suggest that the Rakhiot-Liachar thrust may have been active in uplifting partially molten crust since Miocene time (*42*, *63*). If accelerated uplift due to movement on the Rakhiot-Liachar thrust played a role in the ~1-Ma acceleration of exhumation, then such movement should be linked to increased E-W contraction, uplift, and, ultimately, mass influx to the base of the NPM. Uplift of the NBM in the eastern syntaxis appears to be accommodated by northwest-directed thrust faults on its northwestern margin based on earthquake focal mechanisms (*59*, *70*). The nearly synchronous timing of accelerated exhumation of young, hot middle crust in both syntaxial massifs (Fig. 7) may therefore reflect (i) a plate-scale geometric change in the orogen that accelerated mass input into the syntaxes and/or (ii) a structural control on mass input into the syntaxes.

Recent geodynamic and geophysical modeling studies suggest that uplift and mass influx to the base of the massif may be linked to the 3D geometry of the plate margin, specifically as a consequence of the development of the arcuate shape of the Himalaya. Geometric stiffening at the corners of a curved down-going plate in an arcuate convergent boundary (such as the Himalaya) is a natural consequence of its geometry, that is, geometric stiffening at the plate corners produces an orogen-normal, antiformal asperity on the down-going plate (*12*). Geodynamic models show that underthrusting of such a rigid asperity can induce localized uplift and ultrafast exhumation of the upper plate (*12*). However, this model fails to account for the exhumation of lower-plate (Indian plate) crust in the syntaxes (*63*).

Another mechanism proposed to drive mass input and uplift in the syntaxes is orogen-parallel crustal flow (*11*, *71*). In this mechanism, strain partitioning that originates from along-strike changes in convergence obliquity due to the curvature of the orogen causes

orogen-parallel crustal flow and vertical extrusion in the syntaxes. Thus, changes in convergence obliquity due to changes in the 3D orientation of the orogen may accelerate orogen-parallel crustal flow, triggering localized ultrafast exhumation in the syntaxes.

Alternatively, an acceleration of exhumation at 1 Ma in the syntaxes may simply be a consequence of structurally controlled crustal velocity during orogen-parallel crustal flow. The Rakhiot-Liachar thrust is steeply dipping, and its geometry below ~10 km is unknown. If connected to a shallow-dipping basal detachment, then the phase of slower exhumation from 4 to 1 Ma (~2 to 4 mm/year) revealed by our data could be interpreted to track crustal flow along the shallow-dipping basal detachment. A change from flow along this detachment to nearly vertical flow along the Rakhiot-Liachar thrust in the NPM would manifest in the rock record as acceleration to ultrafast exhumation without any change in the rate of crustal flow. Thus, the 1-Ma acceleration in exhumation may track a change from predominantly horizontal flow at midcrustal depths to nearly vertical flow along the Rakhiot-Liachar thrust in the NPM. An implication of this structural control is that earlier-exhumed rocks in the outer margins of the NPM would all have experienced a late-stage acceleration in exhumation during their ascent to the surface throughout the evolution of the NPM; whether or not this would be preserved in the rock record is unclear. Our petrochronologic data cannot distinguish between orogen-scale geometric changes or structurally controlled crustal flow as the main reason for the observed ~1-Ma pulse of exhumation in the NPM. However, the broader geologic constraints discussed above and in the preceding sections suggest that this modern pulse of accelerated exhumation was dominantly influenced by tectonics.

In summary, our study reveals diachronous melting and crystallization histories between different rocks in the NPM, as well as a pulse of ultrafast (9 to 13 mm/year) exhumation that began ~1 Ma, which was preceded by slower exhumation (2 to 4 mm/year). Our data, combined with results of studies that show a similar pulse of ultrafast exhumation in the NBM, suggest that neither surficial processes (fluvial and/or glacial erosion) nor crustal melting was the dominant trigger for accelerated exhumation at ~1 Ma. Results from 1D thermal modeling are consistent with slower, but still rapid, crustal extrusion in the NPM preceding the ~1-Ma ultrafast exhumation by several million years. The data do not indicate whether or not the Tectonic Aneurysm mechanism was responsible for initial exhumation of the NPM. Rather, our study, combined with results of recent studies, collectively suggests that the current tempo of rapid exhumation in the Himalayan syntaxes is relatively insensitive to changes in the efficacy of surface denudation and is ultimately dictated by tectonic or structural forcing.

MATERIALS AND METHODS

Samples, petrography, and imaging

Both of the studied samples were collected as float from the upper reaches of the Rakhiot glacier by M. P. Searle in 1994. Polished thin sections were made and used for petrographic and electron beam analysis and imaging. Two thin sections for sample K-94-30 and one thin section for sample K-94-29 were used for this study. Mineral textures and assemblages in each thin section were characterized using optical and electron microscopy. Full thin section element maps of Ca, Mg, Mn, K, Na, P, Si, Ti, Y, and Zr, as well as element maps of Ca, Mg, Fe, Mn, and Cr of individual garnet crystals in both samples were made using a combination of energy-dispersive spectrometry (EDS hypermapping) and wavelength-dispersive spectroscopy (WDS) with the CAMECA SX*five*-TACTIS at University of Massachusetts, Amherst. These maps were done at 15 kV, 200 nA, and 35 μm beam diameter using a stage step size of 35 μm and a pixel dwell time of 25 ms. Garnet grains in both samples were mapped for major elements (Ca, Fe, Mg, and Mn) by integrated EDS (extracted from hypermaps) and Cr by WDS on the CAMECA SX*five*-TACTIS at University of Massachusetts, Amherst. These garnet maps were done at 15 kV and 300 nA with 200 ms/pixel. Cr was collected on two spectrometers, and counts were integrated in a final map. Using full thin section element maps and back-scattered electron images, monazite grains were located and mapped for Y, Th, and Ca zoning using WDS on a combination of the following electron microprobes: (i) CAMECA SX-50 at Virginia Tech with an accelerating voltage of 15 kV, a current of 200 nA, and a dwell time of 30 ms/pixel; (ii) CAMECA SX-100 at Rensselaer Polytechnic Institute with an accelerating voltage of 15 kV, a current of 200 nA, and a dwell time of 30 ms/pixel; and (iii) CAMECA SX*five*-TACTIS at University of Massachusetts, Amherst at 15 kV, 200 nA (focused beam), 100 ms/pixel, and 05-μm step size. In addition, monazite and garnet x-ray maps were processed in ImageJ. Phase maps of various textures were made by combining and processing EDS major element maps collected on a Zeiss Evo 50 scanning electron microscope outfitted with an Oxford Instruments X-MAX EDS detector in the software AZtec (Oxford Instruments) at Amherst College.

Phase equilibria modeling

The exhumation rates determined from monazite petrochronology are dependent on the amount of decompression recorded by the studied samples. We tested the sensitivity of calculated phase equilibria (and thus the inferred pressures of different reactions and amount of decompression of the inferred *P-T* path) presented in (*4*) to (i) the use of different thermodynamic datasets and solution models and (ii) addition of MnO to the bulk composition, as this would be expected to stabilize garnet to lower pressures and temperatures (*72*). We recalculated phase equilibria for the bulk composition of sample K-94-29 from (*4*) in the system Na_2O-CaO-K_2O-FeO-MgO-Al_2O_3-SiO_2-H_2O ± MnO in Perple_X version 6.8.3 (*39*, *40*). To assess the sensitivity of calculated phase equilibria to different thermodynamic data and solution models, we performed calculations using three different combinations of thermodynamic datasets and solution models (table S1). The pseudosections presented in (*7*) were calculated in an MnO-free system. No constraints on the bulk-rock MnO composition for sample K-94-29 currently exist. To assess the sensitivity of calculated phase equilibria to the addition of MnO to the system, pseudosections were made for the bulk composition of K-94-29: (i) without MnO and (ii) with addition of MnO in two amounts: 0.1 and 0.5 mol %, with the latter value being a likely maximum bulk-rock MnO concentration (*72*). The results of our recalculated phase equilibria models are shown in fig. S4.

Monazite petrochronology

Analyses of U, Th, and Pb isotopes and trace elements in monazite were carried out via laser-ablation split-stream inductively coupled mass spectrometry (ICP-MS) at the University of California, Santa Barbara following the methodology in (*41*). Laser ablation was done on a Photon Machines Excite 193 excimer ArF laser-ablation system with a HeLex sample cell. The aerosol stream was split; part of

it was directed to a Nu plasma high-resolution multicollector ICP-MS for U, Th, and Pb isotopic analyses, while the other part was directed to an Agilent 7700 quadrupole ICP-MS for trace element analyses. Spot diameters were 8 μm and were ablated during a 15-s analysis at 4 Hz and ~1 J/cm^2. Sample analyses involved a 15-s baseline measurement approximately every 8 to 10 analyses. Monazite reference materials (RMs) were analyzed every 8 to 10 analyses. 44069 (424 Ma) (*73*) was used as a primary RM to correct for mass bias and downhole fractionation; FC-1 (*74*) (55.7 Ma) (*74*) and Bananeira (512 Ma) (*73*) were used to monitor the accuracy of isotopic data. All RMs in the analytical session gave weighted mean ages that are within ~2% of their published ages. Repeat analyses of 44069 gave a weighted mean age of 425 ± 4.7 Ma (n = 25), those of FC-1 gave a weighted mean age of 56.9 ± 0.5 Ma (n = 8), and those of Bananeira gave a weighted mean age of 510 ± 2.8 Ma (n = 24). Bananeira was used as the primary trace element RM; P was used as the internal standard and assumed to be 12.9% in unknowns. Data reduction was carried out using Iolite version 2.5, and age versus trace element concentration plots were made in MATLAB. All uncertainties are given at 2σ.

In young (younger than Miocene) rocks, ^{206}Pb/^{238}U dates give apparently older crystallization ages due to secular isotopic disequilibrium induced by short-lived ^{230}Th in the ^{238}U decay chain (*75*). Moreover, low concentrations of radiogenic ^{207}Pb result in imprecise ^{207}Pb/^{235}U dates, and high Th concentrations of monazite result in relatively high concentrations of radiogenic ^{208}Pb compared to background or common Pb. Because of the exceptional youth of the samples analyzed in this study (and thus low accumulated radiogenic ^{208}Pb), we applied a ^{204}Pb-based blanket common Pb correction to all analyses and used the common Pb–corrected ^{208}Pb/^{232}Th dates for petrochronologic interpretation.

To reduce the dimensionality of the monazite trace element data and identify critical compositional vectors, we performed a PCA [e.g., (*76*)]. For each sample, all monazite trace element concentrations were transformed using a centered log-ratio transformation (*77*) that accords equal status to each of the trace elements considered. Before normalization, a constant-sum constraint was imposed on each spot analysis through the addition of a residual variable. All PCA calculations were implemented using the princomp function in MATLAB. Factor loadings are displayed in fig. S8.

Thermal modeling

A simple, 1D thermal model was used to examine the evolving thermal structure of the sub-NPM crust over the past 10 Ma. The fully explicit finite difference conduction model used a discretized 22-km-thick column of crust with a node spacing of 0.05 km and time steps of 20 years. The temperatures of the top and base of the model were fixed at 0° and 750°C, respectively, and heat was added to the column assuming a constant radiogenic heat production of 3 μW/m^3, density of 2.8 g cm^{-3}, and heat capacity of 1000 J kg^{-1} K^{-1} throughout. The thermal field was advected upward at imposed exhumation rates, with conduction of heat throughout the column also calculated at each time step. We considered a series of exhumation rates for each of three time intervals (10 to 4, 4 to 1, and 1 to 0 Ma), calculating how the thermal field would evolve in response to each. In each model, we calculated a *P-T* path for a rock that would appear at the bottom of the model crustal column (22-km depth) at a time that would result in it reaching 0-km depth at the end of the simulation.

SUPPLEMENTARY MATERIALS

Supplementary material for this article is available at https://science.org/doi/10.1126/sciadv.abm2689

View/request a protocol for this paper from *Bio-protocol*.

REFERENCES AND NOTES

1. S. K. Mandal, D. Scherler, H. Wittmann, Tectonic accretion controls erosional cyclicity in the Himalaya. *AGU Adv.* **2**, e2021AV000487 (2021).
2. J. A. Spotila, A. L. Berger, Exhumation at orogenic indentor corners under long-term glacial conditions: Example of the St. Elias orogen, Southern Alaska. *Tectonophysics* **490**, 241–256 (2010).
3. P. K. Zeitler, A. S. Meltzer, P. O. Koons, D. Craw, B. Hallet, C. P. Chamberlain, W. S. Kidd, S. K. Park, L. Seeber, M. Bishop, Erosion, Himalayan geodynamics, and the geomorphology of metamorphism. *GSA Today* **11**, 4–9 (2001).
4. J. L. Crowley, D. J. Waters, M. P. Searle, S. A. Bowring, Pleistocene melting and rapid exhumation of the Nanga Parbat massif, Pakistan: Age and *P–T* conditions of accessory mineral growth in migmatite and leucogranite. *Earth Planet. Sci. Lett.* **288**, 408–420 (2009).
5. P. K. Zeitler, C. P. Chamberlain, H. A. Smith, Synchronous anatexis, metamorphism, and rapid denudation at Nanga Parbat (Pakistan Himalaya). *Geology* **21**, 347–350 (1993).
6. D. A. Schneider, M. A. Edwards, P. K. Zeitler, C. D. Coath, Mazeno Pass Pluton and Jutial Pluton, Pakistan Himalaya: Age and implications for entrapment mechanisms of two granites in the Himalaya. *Contrib. Mineral. Petrol.* **136**, 273–284 (1999).
7. G. Govin, P. van der Beek, Y. Najman, I. Millar, L. Gemignani, P. Huyghe, G. Dupont-Nivet, M. Bernet, C. Mark, J. Wijbrans, Early onset and late acceleration of rapid exhumation in the Namche Barwa syntaxis, eastern Himalaya. *Geology* **48**, 1139–1143 (2020).
8. G. E. King, F. Herman, B. Guralnik, Northward migration of the eastern Himalayan syntaxis revealed by OSL thermochronometry. *Science* **353**, 800–804 (2016).
9. P. O. Koons, P. K. Zeitler, B. Hallet, in *Treatise on Geomorphology*, J. F. Shroder, Ed. (Academic Press, 2013), pp. 318–349.
10. P. Wang, D. Scherler, J. Liu-Zeng, J. Mey, J.-P. Avouac, Y. Zhang, D. Shi, Tectonic control of Yarlung Tsangpo Gorge revealed by a buried canyon in Southern Tibet. *Science* **346**, 978–981 (2014).
11. D. M. Whipp Jr., C. Beaumont, J. Braun, Feeding the "aneurysm": Orogen-parallel mass transport into Nanga Parbat and the western Himalayan syntaxis. *J. Geophys. Res. Solid Earth* **119**, 5077–5096 (2014).
12. R. Bendick, T. A. Ehlers, Extreme localized exhumation at syntaxes initiated by subduction geometry. *Geophys. Res. Lett.* **41**, 5861–5867 (2014).
13. A. Koptev, T. A. Ehlers, M. Nettesheim, D. M. Whipp, Response of a rheologically stratified lithosphere to subduction of an indenter-shaped plate: Insights into localized exhumation at orogen syntaxes. *Tectonics* **38**, 1908–1930 (2019).
14. L. Ding, D. Zhong, A. Yin, P. Kapp, T. M. Harrison, Cenozoic structural and metamorphic evolution of the eastern Himalayan syntaxis (Namche Barwa). *Earth Planet. Sci. Lett.* **192**, 423–438 (2001).
15. A. G. Whittington, P. J. Treloar, Crustal anatexis and its relation to the exhumation of collisional orogenic belts, with particular reference to the Himalaya. *Mineral. Mag.* **66**, 53–91 (2002).
16. F. S. Spear, M. J. Kohn, Trace element zoning in garnet as a monitor of crustal melting. *Geology* **24**, 1099–1102 (1996).
17. M. J. Caddick, J. Konopasek, A. B. Thompson, Preservation of garnet growth zoning and the duration of prograde metamorphism. *J. Petrol.* **51**, 2327–2347 (2010).
18. L. S. Hollister, Garnet Zoning: An interpretation based on the rayleigh fractionation model. *Science* **154**, 1647–1651 (1966).
19. D. Rubatto, S. Chakraborty, S. Dasgupta, Timescales of crustal melting in the Higher Himalayan Crystallines (Sikkim, Eastern Himalaya) inferred from trace element-constrained monazite and zircon chronology. *Contrib. Mineral. Petrol.* **165**, 349–372 (2013).
20. S. Prowatke, S. Klemme, Trace element partitioning between apatite and silicate melts. *Geochim. Cosmochim. Acta* **70**, 4513–4527 (2006).
21. J. M. Pyle, F. S. Spear, R. L. Rudnick, W. F. McDonough, Monazite–xenotime–garnet equilibrium in metapelites and a new monazite- garnet thermometer. *J. Petrol.* **42**, 2083–2107 (2001).
22. G. R. Watt, High-thorium monazite-(Ce) formed during disequilibrium melting of metapelites under granulite-facies conditions. *Mineral. Mag.* **59**, 735–743 (1995).
23. C. Yakymchuk, C. L. Kirkland, C. Clark, Th/U ratios in metamorphic zircon. *J. Metamorph. Geol.* **36**, 715–737 (2018).
24. R. M. Holder, B. R. Hacker, A. R. C. Kylander-Clark, J. M. Cottle, Monazite trace-element and isotopic signatures of (ultra)high-pressure metamorphism: Examples from the Western Gneiss Region, Norway. *Chem. Geol.* **409**, 99–111 (2015).
25. J. F. Shroder, M. P. Bishop, Unroofing of the Nanga Parbat Himalaya. *Geol. Soc. Spec. Publ.* **170**, 163–179 (2000).

26. R. M. Palin, O. M. Weller, D. J. Waters, B. Dyck, Quantifying geological uncertainty in metamorphic phase equilibria modelling; a Monte Carlo assessment and implications for tectonic interpretations. *Geosci. Front.* **7**, 591–607 (2016).
27. A. E. Blythe, D. W. Burbank, A. Carter, K. Schmidt, J. Putkonen, Plio-Quaternary exhumation history of the central Nepalese Himalaya: 1. Apatite and zircon fission track and apatite [U-Th]/He analyses. *Tectonics* **26**, TC3002 (2007).
28. R. C. Thiede, T. A. Ehlers, Large spatial and temporal variations in Himalayan denudation. *Earth Planet. Sci. Lett.* **371-372**, 278–293 (2013).
29. D. Craw, P. O. Koons, D. Winslow, C. P. Chamberlain, P. Zeitler, Boiling fluids in a region of rapid uplift, Nanga Parbat Massif, Pakistan. *Earth Planet. Sci. Lett.* **128**, 169–182 (1994).
30. D. M. Winslow, P. K. Zeitler, C. P. Chamberlain, L. S. Hollister, Direct evidence for a steep geotherm under conditions of rapid denudation, Western Himalaya, Pakistan. *Geology* **22**, 1075–1078 (1994).
31. P. K. Zeitler, P. O. Koons, M. P. Bishop, C. P. Chamberlain, D. Craw, M. A. Edwards, S. Hamidullah, M. Q. Jan, M. A. Khan, M. U. K. Khattak, W. S. F. Kidd, R. L. Mackie, A. S. Meltzer, S. K. Park, A. Pecher, M. A. Poage, G. Sarker, D. A. Schneider, L. Seeber, J. F. Shroder, Crustal reworking at Nanga Parbat, Pakistan: Metamorphic consequences of thermal-mechanical coupling facilitated by erosion. *Tectonics* **20**, 712–728 (2001).
32. P. O. Koons, P. K. Zeitler, C. P. Chamberlain, D. Craw, A. S. Meltzer, Mechanical links between erosion and metamorphism in Nanga Parbat, Pakistan Himalaya. *Am. J. Sci.* **302**, 749–773 (2002).
33. G. V. Depine, C. L. Andronicos, J. Phipps-Morgan, Near-isothermal conditions in the middle and lower crust induced by melt migration. *Nature* **452**, 80–83 (2008).
34. V. M. Tiwari, D. C. Mishra, A. K. Pandey, The lithospheric density structure below the western Himalayan syntaxis: Tectonic implications. *Geol. Soc. Spec. Publ.* **412**, 55–65 (2015).
35. C. Lin, M. Peng, H. Tan, Z. Xu, Z.-H. Li, W. Kong, T. Tong, M. Wang, W. Zeng, Crustal structure beneath Namche Barwa, eastern Himalayan syntaxis: New insights from three-dimensional magnetotelluric imaging. *J. Geophys. Res. Solid Earth* **122**, 5082–5100 (2017).
36. L. S. Hollister, D. Grujic, Pulsed channel flow in Bhutan. *Geol. Soc. Spec. Publ.* **268**, 415–423 (2006).
37. H. Ding, Z. Zhang, M. J. Kohn, Z. Gou, Timescales of partial melting and melt crystallization in the Eastern Himalayan Orogen: Insights from zircon petrochronology. *Geochem. Geophys. Geosyst.* **22**, e2020GC009539 (2021).
38. M. J. Streule, M. P. Searle, D. J. Waters, M. S. A. Horstwood, Metamorphism, melting, and channel flow in the Greater Himalayan Sequence and Makalu leucogranite: Constraints from thermobarometry, metamorphic modeling, and U-Pb geochronology. *Tectonics* **29**, TC5011 (2010).
39. M. P. Searle, L. A. Owen, The evolution of the indus river in relation to topographic uplift, erosion, climate and geology of Western Tibet, the trans-himalayan and high himalayan ranges, in *The Indus River: Biodiversity, Resources, Humankind*, A. Meadows, P. S. Meadows, Eds. (Oxford Univ. Press, 1999), pp. 210–230.
40. M. P. Searle, Geological evidence against large-scale pre-Holocene offsets along the Karakoram Fault: Implications for the limited extrusion of the Tibetan plateau. *Tectonics* **15**, 171–186 (1996).
41. R. J. Phillips, R. R. Parrish, M. P. Searle, Age constraints on ductile deformation and long-term slip rates along the Karakoram fault zone, Ladakh. *Earth Planet. Sci. Lett.* **226**, 305–319 (2004).
42. D. A. Schneider, P. K. Zeitler, W. S. F. Kidd, M. A. Edwards, Geochronologic constraints on the tectonic evolution and exhumation of Nanga Parbat, Western Himalaya Syntaxis, revisited. *J. Geol.* **109**, 563–583 (2001).
43. G. Foster, D. Vance, T. Argles, N. Harris, The Tertiary collision-related thermal history of the NW Himalaya. *J. Metamorph. Geol.* **20**, 827–843 (2002).
44. F. Chirouze, P. Huyghe, C. Chauvel, P. van der Beek, M. Bernet, J.-L. Mugnier, Stable drainage pattern and variable exhumation in the Western Himalaya since the Middle Miocene. *J. Geol.* **123**, 1–20 (2015).
45. F. Herman, D. Seward, P. G. Valla, A. Carter, B. Kohn, S. D. Willett, T. A. Ehlers, Worldwide acceleration of mountain erosion under a cooling climate. *Nature* **504**, 423–426 (2013).
46. S. P. S. Gulick, J. M. Jaeger, A. C. Mix, H. Asahi, H. Bahlburg, C. L. Belanger, G. B. B. Berbel, L. Childress, E. Cowan, L. Drab, M. Forwick, A. Fukumura, S. Ge, S. Gupta, A. Kioka, S. Konno, L. J. LeVay, C. März, K. M. Matsuzaki, E. L. McClymont, C. Moy, J. Müller, A. Nakamura, T. Ojima, F. R. Ribeiro, K. D. Ridgway, O. E. Romero, A. L. Slagle, J. S. Stoner, G. St-Onge, I. Suto, M. D. Walczak, L. L. Worthington, I. Bailey, E. Enkelmann, R. Reece, J. M. Swartz, Mid-Pleistocene climate transition drives net mass loss from rapidly uplifting St. Elias Mountains, Alaska. *Proc. Natl. Acad. Sci. U.S.A.* **112**, 15042–15047 (2015).
47. P. R. Bierman, D. R. Montgomery, *Key Concepts in Geomorphology* (Macmillan Learning, ed. 2, 2020).
48. F. Herman, J.-D. Champagnac, Plio-Pleistocene increase of erosion rates in mountain belts in response to climate change. *Terra Nova* **28**, 2–10 (2016).
49. J. Lai, A. M. Anders, Tectonic controls on rates and spatial patterns of glacial erosion through geothermal heat flux. *Earth Planet. Sci. Lett.* **543**, 116348 (2020).
50. M. F. Azam, J. S. Kargel, J. M. Shea, S. Nepal, U. K. Haritashya, S. Srivastava, F. Maussion, N. Qazi, P. Chevallier, A. P. Dimri, A. V. Kulkarni, J. G. Cogley, I. M. Bahuguna, Glaciohydrology of the Himalaya-Karakoram. *Science* **373**, eabf3668 (2021).
51. D. Wallis, A. Carter, R. J. Phillips, A. J. Parsons, M. P. Searle, Spatial variation in exhumation rates across Ladakh and the Karakoram: New apatite fission track data from the Eastern Karakoram, NW India. *Tectonics* **35**, 704–721 (2016).
52. R. Yang, F. Herman, T. Liu, R. H. Biswas, M. G. Fellin, Y. Tian, J. Gong, R. Jiao, C. Maden, H. Chen, Enhanced Quaternary exhumation in the Namche Barwa syntaxis, eastern Himalaya. *Geology* **49**, 958–962 (2021).
53. C. L. Rosenberg, M. R. Handy, Experimental deformation of partially melted granite revisited: Implications for the continental crust. *J. Metamorph. Geol.* **23**, 19–28 (2005).
54. C. Teyssier, D. L. Whitney, Gneiss domes and orogeny. *Geology* **30**, 1139–1142 (2002).
55. D. Grujic, C. J. Warren, J. L. Wooden, Rapid synconvergent exhumation of Miocene-aged lower orogenic crust in the eastern Himalaya. *Lithosphere* **3**, 346–366 (2011).
56. P. K. Zeitler, C. P. Chamberlain, Petrogenetic and tectonic significance of young leucogranites from the northwestern Himalaya, Pakistan. *Tectonics* **10**, 729–741 (1991).
57. C. Yakymchuk, M. Brown, Consequences of open-system melting in tectonics. *J. Geol. Soc. London* **171**, 21–40 (2014).
58. S. K. Park, R. L. Mackie, Resistive (dry?) lower crust in an active orogen, Nanga Parbat, northern Pakistan. *Tectonophysics* **316**, 359–380 (2000).
59. P. K. Zeitler, A. S. Meltzer, L. Brown, W. S. F. Kidd, C. Lim, E. Enkelmann, in *Toward an Improved Understanding of Uplift Mechanisms and the Elevation History of the Tibetan Plateau*, J. Nie, B. K. Horton, G. D. Hoke, Eds. (Geological Society of America, 2014), vol. 507.
60. Z. Tian, M. Brown, Z. Zhang, P. M. Piccoli, X. Dong, Contrasting CW and CCW tectono-metamorphic belts in the eastern Himalayan syntaxis: Quantification of P–T–t paths and tectonic interpretation. *Gondw. Res.* **79**, 1–26 (2020).
61. T. Peng, A. Gerdes, L. Zeng, L. Millonig, R. Albert, L. Marko, H. Wang, C.-M. Wu, Divergent metamorphism within the Namche Barwa Complex, the Eastern Himalaya, Southeast Tibet, China: Insights from in situ U–Th–Pb dating of metamorphic monazite. *J. Metamorph. Geol.* **40**, 307–328 (2021).
62. A. L. Booth, C. P. Chamberlain, W. S. F. Kidd, P. K. Zeitler, Constraints on the metamorphic evolution of the eastern Himalayan syntaxis from geochronologic and petrologic studies of Namche Barwa. *Geol. Soc. Am. Bull.* **121**, 385–407 (2009).
63. R. W. H. Butler, Tectonic evolution of the Himalayan syntaxes: The view from Nanga Parbat. *Geol. Soc. Spec. Publ.* **483**, 215–254 (2019).
64. R. W. H. Butler, D. J. Prior, R. J. Knipe, Neotectonics of the Nanga Parbat Syntaxis, Pakistan, and crustal stacking in the northwest Himalayas. *Earth Planet. Sci. Lett.* **94**, 329–343 (1989).
65. F. Jouanne, A. Awan, A. Pêcher, A. Kausar, J. L. Mugnier, I. Khan, N. A. Khan, J. Van Melle, Present-day deformation of northern Pakistan from Salt Ranges to Karakorum Ranges. *J. Geophys. Res. Solid Earth* **119**, 2487–2503 (2014).
66. M. P. Searle, T. N. Lamont, Compressional metamorphic core complexes, low-angle normal faults and extensional fabrics in compressional tectonic settings. *Geol. Mag.* **157**, 101–118 (2020).
67. F. Jouanne, N. Munawar, J.-L. Mugnier, A. Ahmed, A. A. Awan, P. Bascou, R. Vassallo, Seismic coupling quantified on inferred décollements beneath the western syntaxis of the Himalaya. *Tectonics* **39**, e2020TC006122 (2020).
68. R. W. H. Butler, M. Casey, G. E. Lloyd, C. E. Bond, P. McDade, Z. Shipton, R. Jones, Vertical stretching and crustal thickening at Nanga Parbat, Pakistan Himalaya: A model for distributed continental deformation during mountain building. *Tectonics* **21**, 9-1–9-17 (2002).
69. R. W. H. Butler, D. J. Prior, Tectonic controls on the uplift of the Nanga Parbat Massif, Pakistan Himalayas. *Nature* **333**, 247–250 (1988).
70. C. Xie, B. Zhou, P. Wang, Z. Li, T. Liu, W. Pang, Z. Cao, The seismogenic structure of the 2017 Mw 6.9 milin, tibet, earthquake: A possible newly active fault at the Eastern Himalayan Syntaxis. *Seismol. Res. Lett.* **93**, 68–75 (2021).
71. L. Seeber, A. Pêcher, Strain partitioning along the Himalayan arc and the Nanga Parbat antiform. *Geology* **26**, 791–794 (1998).
72. R. W. White, R. Powell, T. E. Johnson, The effect of Mn on mineral stability in metapelites revisited: New *a–x* relations for manganese-bearing minerals. *J. Metamorph. Geol.* **32**, 809–828 (2014).
73. J. N. Aleinikoff, W. S. Schenck, M. O. Plank, L. Srogi, C. M. Fanning, S. L. Kamo, H. Bosbyshell, Deciphering igneous and metamorphic events in high-grade rocks of the Wilmington Complex, Delaware: Morphology, cathodoluminescence and backscattered electron zoning, and SHRIMP U-Pb geochronology of zircon and monazite. *Geol. Soc. Am. Bull.* **118**, 39–64 (2006).
74. M. S. Horstwood, G. L. Foster, R. R. Parrish, S. R. Noble, G. M. Nowell, Common-Pb corrected in situ U–Pb accessory mineral geochronology by LA-MC-ICP-MS. *J. Anal. At. Spectrom* **18**, 837–846 (2003).

75. U. Schärer, The effect of initial^{230}Th disequilibrium on young UPb ages: The Makalu case, Himalaya. *Earth Planet. Sci. Lett.* **67**, 191–204 (1984).
76. J. M. Garber, B. R. Hacker, A. R. C. Kylander-Clark, M. Stearns, G. Seward, Controls on trace element uptake in metamorphic titanite: Implications for petrochronology. *J. Petrol.* **58**, 1031–1057 (2017).
77. J. Aitchison, The statistical analysis of compositional data. *J. R. Stat. Soc. B. Methodol.* **44**, 139–160 (1982).
78. J.-P. Burg, P. Bouilhol, Timeline of the South Tibet–Himalayan belt: The geochronological record of subduction, collision, and underthrusting from zircon and monazite U–Pb ages1. *Can. J. Earth Sci.* **56**, 1318–1332 (2018).
79. R. C. Thiede, T. A. Ehlers, B. Bookhagen, M. R. Strecker, Erosional variability along the northwest Himalaya. *J. Geophys. Res. Earth Surf.* **114**, F01015 (2009).
80. K. W. Huntington, A. E. Blythe, K. V. Hodges, Climate change and Late Pliocene acceleration of erosion in the Himalaya. *Earth Planet. Sci. Lett.* **252**, 107–118 (2006).
81. R. W. White, R. Powell, T. J. B. Holland, Progress relating to calculation of partial melting equilibria for metapelites. *J. Metamorph. Geol.* **25**, 511–527 (2007).
82. T. Holland, J. Baker, R. Powell, Mixing properties and activity-composition relationships of chlorites in the system MgO-FeO-Al2O3-SiO2-H2O. *Eur. J. Mineral.* **10**, 395–406 (1998).
83. T. J. B. Holland, R. Powell, An internally consistent thermodynamic data set for phases of petrological interest. *J. Metamorph. Geol.* **16**, 309–343 (1998).
84. A. Benisek, E. Dachs, H. Kroll, A ternary feldspar-mixing model based on calorimetric data: Development and application. *Contrib. Mineral. Petrol.* **160**, 327–337 (2010).
85. T. Holland, R. Powell, Activity-composition relations for phases in petrological calculations: An asymmetric multicomponent formulation. *Contrib. Mineral. Petrol.* **145**, 492–501 (2003).
86. K. Taylor-Jones, R. Powell, The stability of sapphirine + quartz: Calculated phase equilibria in FeO-MgO-Al_2O_3-SiO_2-TiO_2-O. *J. Metamorph. Geol.* **28**, 615–633 (2010).
87. C. J. Wheller, R. Powell, A new thermodynamic model for sapphirine: Calculated phase equilibria in K_2O–FeO–MgO–Al_2O_3–SiO_2–H_2O–TiO_2–Fe_2O_3. *J. Metamorph. Geol.* **32**, 287–299 (2014).
88. R. W. White, R. Powell, G. L. Clarke, The interpretation of reaction textures in Fe-rich metapelitic granulites of the Musgrave Block, central Australia: Constraints from mineral equilibria calculations in the system K_2O–FeO–MgO–Al_2O_3–SiO_2–H_2O–TiO_2–Fe_2O_3. *J. Metamorph. Geol.* **20**, 41–55 (2002).
89. R. Coggon, T. J. B. Holland, Mixing properties of phengitic micas and revised garnet-phengite thermobarometers. *J. Metamorph. Geol.* **20**, 683–696 (2002).
90. R. W. White, R. Powell, T. J. B. Holland, T. E. Johnson, E. C. R. Green, New mineral activity–composition relations for thermodynamic calculations in metapelitic systems. *J. Metamorph. Geol.* **32**, 261–286 (2014).

Acknowledgments: We thank J. Singer, N. Smail, K. Suarez, and R. Tracy for assistance with electron microprobe imaging and M. Fame for GIS assistance with Fig. 1. Editor C.-T. Lee, P. Kapp, and an anonymous reviewer provided thoughtful comments that improved the manuscript. **Funding:** This work was funded by the Amherst College Faculty Research Fund (V.E.G.), Geological Society of America Northeastern Section Student Research Grant (T.O.), and Skidmore College Faculty Development Grant (V.E.G.) **Author contributions:** Conceptualization: V.E.G. Methodology: V.E.G., A.J.S., M.J.C., T.O., L.W., A.R.C.K.-C., and M.J.J. Investigation: V.E.G., A.J.S., M.J.C., T.O., L.W., M.P.S., and D.J.W. Visualization: V.E.G., A.J.S., and M.J.C. Supervision: V.E.G. and M.J.C. Writing—original draft: V.E.G., A.J.S., and M.J.C. Writing—review and editing: V.E.G., A.J.S., M.J.C., M.P.S., D.J.W., T.O., L.W., A.R.C.K.-C., and M.J.J. **Competing interests:** The authors declare that they have no competing interests. **Data and materials availability:** All data needed to evaluate the conclusions in the paper are present in the paper and/or the Supplementary Materials.

Submitted 26 September 2021
Accepted 15 April 2022
Published 5 August 2022
10.1126/sciadv.abm2689